DYNAMIC CHANGES OF WAVES AND CURRENTS OVER THE COLLAPSING SANDBAR OF THE TENRYU RIVER MOUTH OBSERVED DURING TYPHOON T0704

Yoshimitsu Tajima[1], Haijiang Liu[1] and Shinji Sato[1]

Abstract

This paper studies on interactions between morphological changes and wave and current fields around the Tenryu River mouth during a severe storm. Installing six cameras, authors successfully captured collapse of sand bar around the Tenryu River mouth when typhoon T0704 hit the Pacific Coast of Japan in July 2007. Obtained images were analyzed based on several image processing techniques and, coupled with the other hydrodynamic data, showed clear evidence for interactive features of bathymetry changes and surrounding wave and current fields. Finally, a numerical model based on depth-integrated non-linear shallow water equations and energy balance equations were applied to the observed conditions and it was found that topography changes during the storm was one of the most essential factors that determine the characteristics of surrounding wave and current fields.

Key words: river mouth, sand bar, flood, wave-current interactions, wave breaking, image analysis

1. Introduction

Process-based understandings on dynamic interactions among waves, currents and topography changes around the river mouth are essential to predict the movement of sediments discharged from the river. Especially around the river mouth, river flow, nearshore currents and waves interact with each other and cause complex topography changes. Topography change also affects the surrounding current wave fields. It is virtually difficult to directly observe such features by installing conventional instruments since severe forces induced by flooding current and broken waves dramatically change the bed conditions.

Using multiple cameras, authors successfully captured the collapsing sandbar at the Tenryu River mouth during typhoon T0704 in July 2007. This study aims to explore the interactive characteristics of waves, currents and topography changes around the river mouth based on analysis of obtained images, several hydrodynamic data, and numerical analysis.

2. Observation of Sand Bar Collapse Based on Obtained Images

As seen in Figure 1, six cameras were installed around the Tenryu River mouth. Arrows in the figure respectively indicate directions of the fixed angles of installed cameras. All cameras captured snap-shot images at every 1.2 seconds and recorded these images in a connected hard disk. Following the procedures outlined below, all snap-shot images were rectified and, based on the actual coordinates, multiple images obtained from different cameras were combined to get a top-view-images of the entire river mouth.

In order to exclude instantaneous fluctuations in the image, ten-minute-averaged images were first obtained by averaging RGB-values in each pixel over multiple images within 10 minutes. The ten-minute-averaged images were then rectified based on the coordinates of the real world. According to Holland et al. (1997), geometrical relationship between pixel coordinates of the image, u_i (i=1,2), and real world coordinates, x_j (j=1,2,3), are expressed by

[1]Dept of Civil Eng., The University of Tokyo, 7-3-1 Hongo, Bunkyo-ku, Tokyo 113-8656, Japan. yoshitaji@coastal.t.u-tokyo.ac.jp
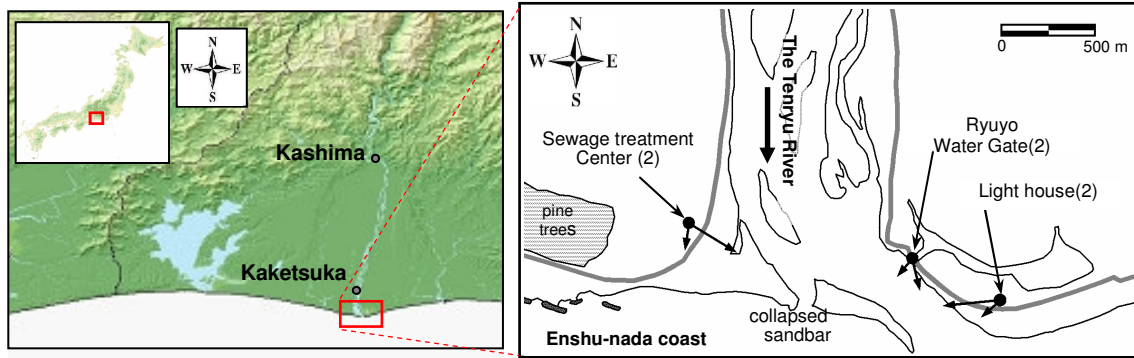
Figure 1 Overview of the Tenryu River mouth and locations and angles of installed six cameras (arrows).

$$u_{*i} = (u_i - u_{0i}) = -f_i \frac{m_{ij}(x_j - x_{cj})}{m_{3j}(x_j - x_{cj})} - k_1 r^2 (u_i - u_{0i}) - k_2 r (u_i - u_{0i}) \tag{1}$$

with f_i, effective focal length combined with scale factors in horizontal and vertical directions, respectively, u_{0i}, center-coordinates of the image and m_{ij}, coefficients determined as functions of camera angles, ϕ_k (k=1,2,3), and position of the camera, x_{cj}. The second and third terms of RHS of equation (1) determine the image distortion dependent on specific lens conditions with r, on-image distance of each pixel from the image-center and the coefficients k_1 and k_2. These coefficients were first determined using the test-image with all the other parameters fixed. Using these determined k_1 and k_2, next, all the other parameters, f_i, ϕ_k, and x_{cj} were calibrated based on the on-site actual image so that equation (1) with determined parameters best-fits the several benchmark points whose coordinates measured by GPS. These optimum parameter-values were iteratively determined from the following the first-order Taylor series of (1).

$$\Delta u_{*i} = \alpha_{ij} \Delta x_{cj} + \beta_{ij} \Delta \phi_k + \gamma_{ij} \Delta f = \frac{\partial u_{*i}}{\partial x_{cj}} \Delta x_{cj} + \frac{\partial u_{*i}}{\partial \phi_k} \Delta \phi_k + \frac{\partial u_{*i}}{\partial f} \Delta f \tag{2}$$

At each benchmark point, pixel coordinates and its derivatives, α_{ij}, β_{ij}, and γ_{ij} are predicted from (1) with previously determined parameters and known coordinates of the real world. Introducing computed α_{ij}, β_{ij}, and γ_{ij} and predicted pixel coordinates in (2), modification of parameters, Δx_{cj}, $\Delta \phi_k$ and Δf, are computed using the least square method. Modified parameters are then applied again to (1) to repeat all the procedures until the estimated errors of image coordinates reach certain expected criteria. Since there are seven unknown parameters, we require at least four bench marks that gives eight separate equations of (2).

While this method minimizes the rms-error of image coordinates at all the benchmark points, it may underestimate the error of real coordinates of the benchmark points if it is located further from the camera than the others since the rate at which real coordinates changes per unit pixel coordinates is larger if the point is further from the camera. Since our goal is to estimate the real coordinates from the image, we introduced a following weight function that is multiplied to both sides of equation (2) before least square method is applied.

$$W_i = \left| \nabla u_i \right|^{-1} \tag{3}$$

Here ∇ is a vector differential operator of the real world coordinates. Figure 2 compares the rectified images with or without the weight function. A white line in the figure indicates a boundary of the shoreline measured by GPS. As expected, the weight function improves the predictive skills of actual coordinates especially around the east end of the sand bar where is further from the camera.

Finally, rectified images taken from the different cameras were combined based on the estimated coordinates. Figures 3 compare four representative combined images of the sand bar topography during the storm. Figures indicate the time at which the images were taken. At 17:00 on July 14th, sand bar showed

initial shape before the river flow increases. At 12:00 on July 15th, sand bar first emerged after the water level at the river mouth passed its peak. East end of the sand bar was collapsed and the opening of the river mouth was significantly widened. At 14:00, middle-west part of the sand bar, at around X=400m, began to collapse and darker outflow was observed in the seaside of the collapsed sand bar. At 17:00, this collapsing middle-west part of the sand bar was fully opened and upstream side of the shoreline along the sandbar clearly retreated. It is interesting to note that the sand bar collapse was observed at two different locations, i.e., the one at east end opening and the other at the middle-west part of the sand bar, and there was certain time-lag between these two collapses.
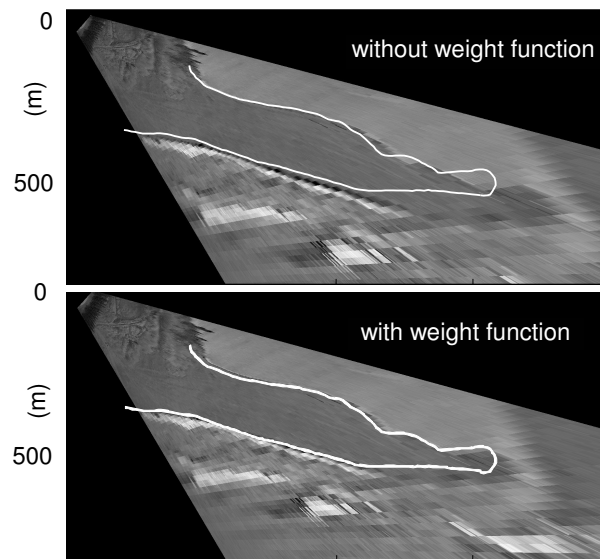
Figure 2 Rectified images with or without weight function. White line is measured boundary of the sandbar.
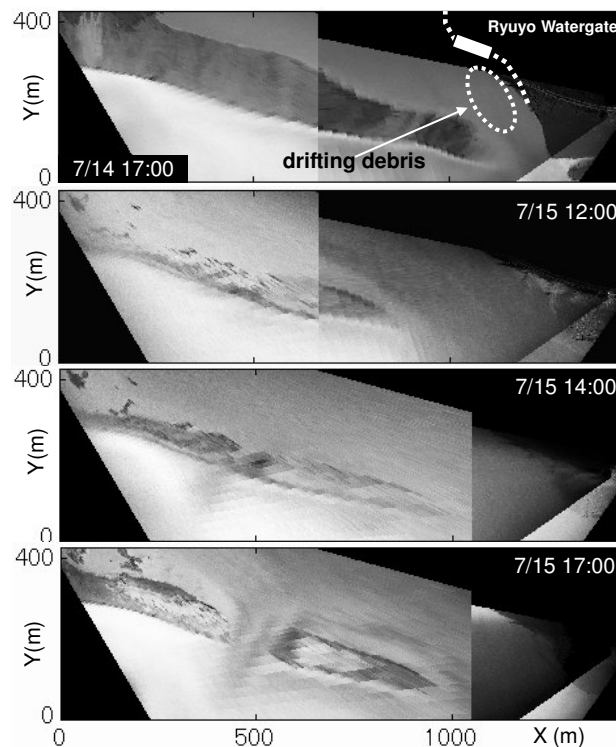
Figures 3 Rectified and combined top-view images of the Tenryu River mouth.

3. Hydrodynamic Characteristics during the Storm

As observed in Figures 3, the storm widened the original river mouth and also cut the middle west part of the sand bar while these two events occurred at different time. This section investigates hydrodynamic characteristics during the storm.

Figure 4 shows the time-series of flow rate at Kashima, surface water levels at Kaketsuka, η_K, Ryuyo, η_R, and offshore, η_O, surface water velocities at Ryuyo, and measured wave heights and periods at offshore. Blank circles are estimated surface water velocity discussed later. Kashima and Kaketsuka are the locations along the Tenryu River and their distance from the river mouth are 25km and 3km, respectively. As shown in Figure 1, Ryuyo is at the water gate behind the sand bar. The river flow rate at Kashhima was estimated based on measured surface water elevations and empirically obtained H-Q curves at Kashima. Since there is no major inflows from Kashima to the river mouth, the flow rate at Kashima should be nearly equivalent to the one around the river mouth although there should be certain time lags. The offshore water level and wave characteristics are based on the data recorded by the wave gauge installed around 5km offshore from the river mouth with water depth of h=40m.

As seen in Figure 4, the peak of the surface water level at Kaketsuka is about four hours later than the one at Kashima. On the other hand, the water level at Ryuyo, which is just behind the sand bar of the river mouth, is clearly affected by tide and therefore the water level at Ryuyo reaches to its peak earlier than the surface water level peak at Kashima. Figure 4 also compares the water level difference between Ryuyo and the offshore, $\Delta\eta=\eta_R-\eta_O$. As seen in this comparison, even the peak of $\Delta\eta$, which excluded the influence of tide, is about two hours earlier than the peak of the surface water level at Kaketsuka. These features may be because: (a) widened river mouth decreased flow velocity and corresponding bottom friction forces; (b) wave heights and corresponding radiation stress had decreased and thus the wave setup had been lowered; and (c) cross-sectional area of the river flow was increased due to elevated water level.

Surface water velocities shown by solid circles in Figure 4 were determined as a velocity of drifting debris such as a piece of wood. Time-varying spatial positions of the debris were first traced from series of successive still images in terms of pixel coordinates. Tracks of drifting debris were transferred to the coordinates of the real world based on equation (1) with already obtained rectification parameters. Finally,
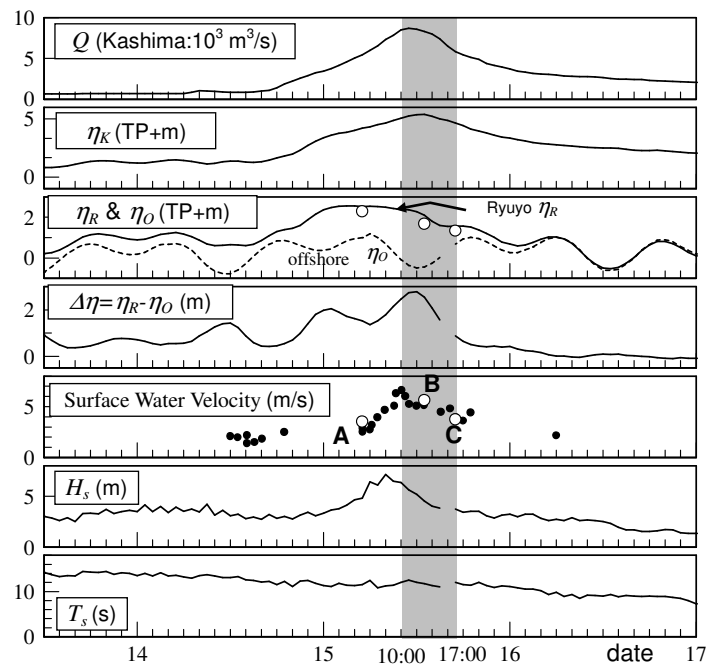
Figures 4 Measured flow rate at Kashima (10^3m^3/s), surface water levels (m) at Kaketsuka(η_K), Ryuyo(η_R) and offshore (η_O), surface water velocities (m/s) at Ryuyo, and measured wave conditions at offshore. Blank circles are results of the present numerical computations.

the distance of the coordinates of the identical debris in two successive images yields instantaneous velocity of the debris. The estimated instantaneous velocities of debris were averaged for five minutes over the area specified in Figure 2 to represent "river mouth velocity." Twelve benchmarks were applied to find the optimum rectification parameters and the rms-error of the actual and rectified distances of each two of these benchmarks were around 4.6%. Since the debris velocity is estimated as a distance between two successive positions of debris, the error of estimated velocity should also be of the same order. The estimated surface water velocity showed characteristic behavior during the storm and the hatched rectangular area in the figure indicate the time between 10:00 to 17:00 on 15th for which we further investigate the physical phenomena with numerical analysis discussed later.

While the surface water velocity at the river mouth also increases with the surface water level, the velocity reaches its peak around 10:00 on 15th, which is about two hours earlier than the peak of $\Delta\eta$, the water level difference between Ryuyo and the offshore. This peak-time of the surface water velocity surely corresponds to the time at which the river mouth opening was severely widen, i.e., intensive hydrodynamic force began to erode the east end of the sand bar. After the peak, surface water velocity appears to stay for six to seven hours and then again abruptly decreases at around 18:00. The timing of this clear decrease of the velocity also corresponds to the time at which the middle-west part of the sand bar was cut.

4. Influence of the River Mouth Morphology on Tidal Response

Figures 3 and 4 clearly indicated that river mouth topography has significant influence on the surrounding current conditions. This section investigates the influence of the bathymetry change on the tidal response around the river mouth based on measured surface water fluctuations before and after the storm.

Figure 5 (a) shows a time-series of tides at Ryuyo and Omaezaki for 40 days around the storm. Omaezaki is on the Enshu-nada coast and about 40km east from the Tenryu River mouth. Tidal data at Omaezaki was selected because the wave gauge at the offshore of the river mouth failed to record continuous data during the storm and daily tidal characteristics observed at this wave gauge before the storm were nearly equivalent to the one at Omaezaki in terms of phase and tidal peaks. The hatched rectangular areas in Figure 5 indicate the target 15-day-periods before and after the storm from which several tidal characteristics were extracted and compared in the following figures. Figure 5 (b) compares peak water levels both during high and low tides at Ryuyo, η_{PR}, and Omaezaki, η_{PO}. Figure 5 (c) shows the time-lags of tidal peaks between Ryuyo and Omaezaki as a function of peak tidal level at Omaezaki, η_{PO}. In these figures, a harmonic analysis was applied respectively to each tidal profile in hatched period of 15 days to estimate accurate surface water level and time at the tidal peaks.

Before the storm, as seen in these figures, the difference of peak water levels at Ryuyo and Omaezaki increases as high as 25 cm as the tidal water level lowers while this difference decreases and eventually
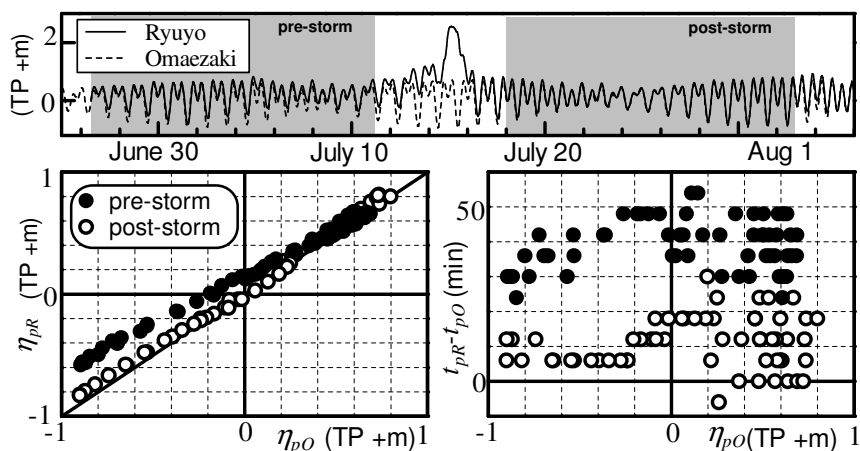
Figure 5 (a) Time-averaged surface water fluctuations at Ryuyo and Omaezaki for 40 days around the storm. (b)Comparisons of peak water level at Ryuyo, η_{PR}, and Omaezaki, η_{PO}, during high and low tide. (c) Time-lags of tidal peaks between Ryuyo and Omaezaki as a function of η_{PO}.

nearly diminishes as the water level reaches to high tide. The time-lag of the tidal peaks at Omaezaki and Ryuyo ranges from 20 to 50 minutes and observed time-lags were shorter during the low tide compared to the high tide. After the storm, on the other hand, the tidal profile at Ryuyo and Omaezaki were similar to each other and their peak-time-lag decreases and ranges from 0 to 30 minutes.

5. Numerical Analysis

As discussed in the previous sections, the river mouth topography showed significant influence on surrounding hydrodynamic characteristics. This section further investigates the hydrodynamic features around the Tenryu River mouth through numerical analysis. Since the waves encounter a relatively strong current around the river mouth, the numerical analysis should account for various features due to wave-current interactions, such as Doppler effects of currents on waves, wave-induced forces acting on currents, and turbulence within bottom boundary layers under wave-current coexisting fields.

5.1. *Model descriptions*

As discussed above, the model should be able to account for various hydrodynamic features due to wave-current interactions. On the other hand, the model should also require computational efficiency so that it can accommodate computations of wave and currents around collapsing river mouth whose spatial scales can be as large as several kilometers and time scales should be of the order of several days or longer. Taking these requirements into account, this study applied following modified wave action balance equations proposed by Mase et al. (2004).

$$\frac{\partial Nc_x}{\partial x}+\frac{\partial Nc_y}{\partial y}+\frac{\partial Nc_\theta}{\partial \theta}=-D_{NB}+\frac{\kappa}{2\sigma}\left[\frac{\partial}{\partial y}\left(CC_g\cos^2\theta\frac{\partial N}{\partial y}\right)-\frac{1}{2}CC_g\cos^2\theta\frac{\partial^2 N}{\partial y^2}\right] \quad (3)$$

Here $N=(S/\sigma)$ is a wave action of each wave frequency, x and y are horizontal axis, θ is an angle of wave specter, c_x, c_y, and c_θ are velocity at which the wave action is transported in the directions of x, y, and θ, respectively, D_{NB} is a dissipation rate of the wave action, κ (=2.5) is a coefficient introduced by Mase et al. (2004), σ is the intrinsic wave frequency relative to the current. This phase-averaged wave model efficiently computes deformations of random wave field accounting for wave shoaling, refraction, diffractions under waves-current coexisting field. Especially for application of the model to the river mouth, breaking and broken wave phenomena predominantly determine the wave and wave-induced current fields. For instance, opposing current against waves break urges more wave breakings, and breaking and broken waves yield intensive radiation forces and turbulence that should have significant impacts on the nearshore current. This study applied Tajima and Madsen's (2005) breaking and broken wave model since the model is capable of predictions of the recovery of broken waves. Since the model is developed so that predicted wave energy agrees well with measured data, moreover, we can expect that the model to yield reasonable radiation forces that predominantly determine the horizontal forcing balance around the river mouth. Following Tajima and Madsen (2005), the broken wave dissipation rate of the wave action, D_{NB} is determined by

$$D_{NB}=-K_b\sqrt{g/h}\exp\left(-\xi_b^2\right)N\left[\left(1+\xi_b^2\right)-E_r/E\right] \quad (4)$$

Here $\xi_b=H/H_b$ is a ratio of local and breaking wave height, H and H_b, $E=\rho g H^2/8$ is the wave energy of the entire specter and $E_r=\rho g H_r^2/8$ is an energy of recovered non-breaking waves whose wave height, H_r, is known to be proportional to the local water depth, h, i.e., $H_r=\gamma_r h=0.3h$. The coefficient, K_b, is conceptually derived as functions of bottom slope, β, as

$$K_b=\frac{5}{2}\cdot\frac{\gamma_s^2\tan\beta}{\gamma_s^2-\gamma_r^2} \text{ with } \gamma_s=\gamma_r+4\tan\beta=0.3+4\tan\beta \quad (5)$$

The present model also introduced the surface roller model proposed by Tajima and Madsen (2005) to account for volume flux and "radiation forces" that significantly affect nearshore current field. Evolution of the surface roller is thus determined by the following energy balance equations with production term based on broken wave energy.

$$\frac{\partial N_{SR}}{\partial t} + \nabla \left(N_{SR} \mathbf{v_{SR}} \right) = \alpha D_{NB} - K_b \sqrt{g/h} N_{SR} \tag{6}$$

Here $N_{SR}=s_{SR}/\sigma$ is a ratio of "specter" of surface roller and corresponding frequency relative to the current, σ. The velocity vector, $\mathbf{v_{sr}}$, at which the surface roller specter should be transported, follows Mase et al's (2004) model except that a wave phase velocity was applied instead of the group velocity under the assumption that the surface roller should be transported with the wave crest. In the right hand side of equation (6), α specifies a proportion of energy provided to the roller out of entire broken wave dissipation energy. This study followed Tajima and Madsen (2005), who applied $\alpha=1/2$ assuming that only a wave potential energy, which is a half of the entire wave energy under linear wave approximations, should be transported to surface roller energy. The second term of the RHS of equation (6) determines the dissipation of the surface roller energy and this term is consistent to the broken wave dissipation term in (4) in that the dissipation rate is assumed to be proportional to the "excessive energy" above the energy of recovering waves. While the wave energy reaches to E_r when it stops breaking and recovers, surface roller vanishes and thus the "surface roller energy on recovering waves" should be zero and thus the last term in (6) surely proportional to the "excessive surface roller energy." Integrating obtained s_{sr} over the entire frequency and directions, one can estimate the spatial distribution of time-averaged surface roller energy, E_{sr}. Following Tajima and Madsen (2005), time-averaged surface roller area, A_{sr}, is then determined by

$$A_{sr} = \frac{2E_{sr}T}{\rho C} \tag{7}$$

Computations of slowly varying current around the river mouth are based on depth- and time-averaged non-liner shallow water equations combined with external forcing terms due to radiation stresses of waves and surface rollers, horizontal dispersions of currents, and bottom shear stress. Dispersion coefficients were determined as the larger one of either depth-averaged turbulent eddy viscosity or the dispersion coefficients proposed by Larson and Kraus (1991). Larson and Kraus' (1991) dispersion coefficient was developed to represent the wave-induced nearshore current field and is defined as a product of the local wave height and the amplitude of local wave-orbital velocity with calibrated proportional constant. Their dispersion coefficients therefore diminish with wave heights and thus underestimate the dispersive features especially inside the river mouth where waves are nearly dissipated. The model therefore accounted for the influence of the turbulent eddy viscosity induced by bottom shear stresses, which should be dominated behind the sand bar. The present model applied Madsen's (1994) bottom boundary layer model to determine the spatial distributions of bottom shear stress under wave-current coexisting field on a movable bed with specified equivalent bottom roughness. Bed materials around the Tenryu River mouth consist of sand grains with median diameters of $D_{50}=0.3mm\sim0.5mm$ and gravels with diameters in the order of several mm to cm. The model applied several bottom roughness conditions to investigate their impacts on the predicted wave and current fields. Especially on the movable sheet flow bed conditions, the model applied Herrmann and Madsen's (2006) model to determine spatially varying equivalent bottom roughness. Finally, both wave and current models were iteratively applied accounting for interactions of each other until the predicted wave and current fields reach their equilibrium conditions.

5.2. *Model applications to the flooding Tenryu River mouth*

The model was applied to the Tenryu River mouth during the storm when flooding river discharge largely cut the sandbar of the river mouth. The model aims to represent semi-steady state conditions at the following three conditions (cases): (i) at 5:00 on 15th when the water level at Ryuyo reached its peak; (ii) at 13:00 on 15th when the river discharge appeared to reach its peak; and (iii) at 17:00 on 15th when

Table 1 Computational conditions of three cases at different times

Case	i	ii	iii
Time (on July 15th,2007)	5:00	13:00	17:00
Offwhore MWL (m)	1.00	-0.44	0.68
Offshore Hs(m)	4.8	4.5	3.7
Ts (s)	11.5	11.7	12.0
Offshore Wave dir. (deg)	29.0	36.0	24.0
River Discharge (m^3/s)	5447	8682	5823
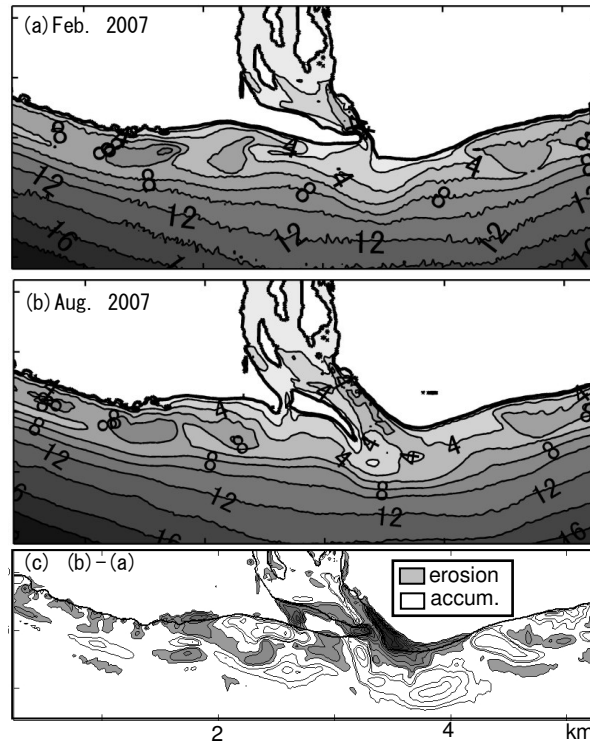
Figure 6 Bathymetry around the river mouth before and after the storm (a and b) and their difference (c).

estimated surface water velocity at the river mouth decreased while the water level at the offshore gauge was as high as the one at 5:00. Table 1 summarizes offshore water level, wave conditions, and river discharge rates respectively for these three cases and these quantities were applied as boundary conditions in the numerical analysis. While the case (ii), at 13:00, applied the peak river discharge rate at Kashima observed at 9:00, the other two cases simply applied the flow rate at Kashima observed at the same time of each case since the time-lag of the flow rate between Kashima and the river mouth was not clearly known. If one were to account for a certain time-lag between Kashima and the river mouth, the discharge rate of case (i) might be slightly smaller than the one in Table 1 since the flow rate in case (i), at 5:00, is in increasing phase and vice-versa in case (iii).

Bathymetry around the river mouth should also have an essential influence on the surrounding wave and current dynamics. Fortunately, two separate bathymetry surveys had been carried out before and after the storm, i.e., the one carried out in February 2007 and the other in August 2007. Figures 6 show these measured bathymetries. Figures 6 also show spatial distributions of the difference of these two water depth. Since the bathymetry under daily wave and current conditions were observed fairy stable especially behind the sandbar, the difference of these two bathymetry should be nearly equivalent to the water-depth change due to the storm, T0704. As seen in these figures, extensive forces during the storm widened and deepened the opening of the river mouth and transported significant amount of sediments to the offshore. Area of the sand deposition, where water depth decreased, is predominantly extended eastward from the offshore of the river mouth. This observed eastward sediment transport is surely consistent with the observed peak wave

direction, SWS, during the storm.

The model aims to compute quasi-steady state conditions at each of three cases and the offshore boundary condition was determined by a constant tidal surface water level as summarized in Table 1. At the both east- and west-side boundaries, the model added 200m-wide imaginary topography with cross-shore profiles represented by the ones at each side and applied open boundary conditions that assume uniformity of all the variables in alongshore directions. Finally, observed river flow rates, outlined in Table 1, were applied at the upstream boundary of the Tenryu River.

Figure 7 shows spatial distributions of predicted wave heights and mean current fields at 13:00 (case ii) when the river discharge rate was at its peak. As seen in the figure, the present model reasonably represents

Table 2 Summary of computed variables

			Symbols	$\Delta\eta$ (m)	u (m/s)
7/15 5:00		measured	—	1.53	2.87
	predicted	(a) bathymetry in Feb. 2007	△	2.71	2.45
		(b) bathymetry in Aug. 2007	▽	0.52	3.22
		(c) bathymetry of 0.5(a)+0.5(b)	○	1.29	3.51
		(d) (c) without wave radiation stress	☐	1.20	3.60
7/15 17:00		measured	●	0.88	3.96
	predicted	(a) k_N=0.5mm	△	0.51	3.86
		(b) k_N=5mm	▽	0.80	3.60
		(c) k_N=50mm	☐	1.24	3.17
		(d) k_N=sheet flow	○	0.66	3.75
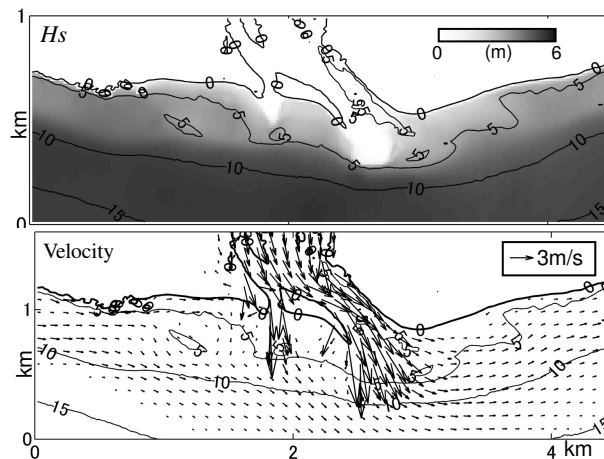
Figure 7 Predicted significant wave heights and depth-averaged mean current velocities (at 13:00; Case ii).
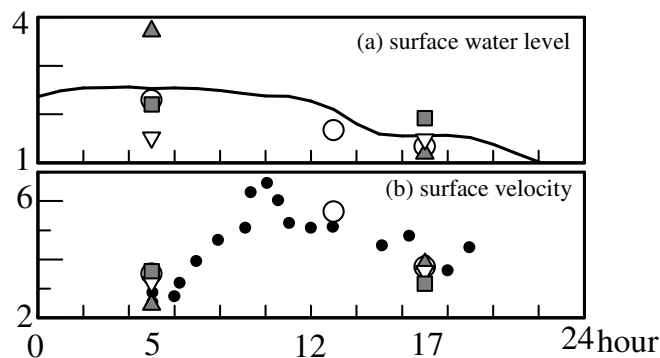
Figure 8 Time-series of recorded surface water level behind the sand bar and surface water velocity at the river mouth compared with predicted values with different computational conditions. Conditions and corresponding symbols are summarized in Table 2.

observed features of wave blocking around the river mouth. Predicted mean current flow abruptly changes its direction eastward as it flows out from the river mouth to encounter the surf zone. This predicted current pattern reasonably explains the observed topography change during the storm, in which discharged sediments were transported eastward and deposited along the surf zone.

To examine the dynamic characteristics of wave-current coexisting field around the river mouth, the model was applied to the cases (i) at 5:00 and (iii) at 17:00 with several different computational conditions indicated in Table 2. Table 2 also summarizes the computed results of: difference of the surface water elevations between the one at Ryuyo water gate just behind the sand bar and the other at the offshore; and mean current velocity at the river mouth. These computed results were also plotted in Figure 8 with time-series of recorded data. Table 2 also indicates the symbols of each case plotted in Figure 8.

Since case (i) at 5:00 is when the river flow discharge is increasing and the sand bar at the river mouth was not yet collapsed, the model was applied to three different bathymetries, i.e., (a) a bathymetry of February 2007, (b) a bathymetry of August 2008 just after the collapse of the sand bar, and (c) an interpolated bathymetry of the one of February and the other of August 2008. The third bathymetry somewhat represents the bathymetry while the sand bar is collapsing during the storm. The model applied Hermann and Madsen's (2006) sheet flow roughness model to represent spatial distributions of equivalent bottom roughness, which yielded reasonable predictive skills in the following investigations. As summarized in Table 2 and Figure 7, difference of the river mouth topography has significant influence on predicted gradient of surface water level. The model, for example, overestimated surface water level at the water gate on the bathymetry of February when the sand bar was well developed while it underestimated on the bathymetry on August when the sand bar was totally collapsed. Applying the water depth between these two bathymetries, the model reasonably predicted the surface water level behind the sand bar.

To examine the influence of wave-induced forces, case (d) applied the same computation conditions of case (c) except the wave radiation forces neglected in the momentum equations. As summarized in Table 2, case (d) predicted the surface water elevation from offshore, $\Delta\eta$, about 9 cm lower than the case (c). This difference, caused by the wave radiation forces, was relatively smaller than those among cases (a), (b), and (c) in which the river mouth bathymetry was altered. River mouth bathymetry therefore has rather significant impact on surrounding hydrodynamics.

As discussed in the previous section, case (i) applied three different bathymetry conditions since the river mouth bathymetry was in the process of collapsing and thus measured bathymetry data before and after the storm do not appropriately represent the bathymetry conditions. In contrast, the case (iii) focuses on the time, 17:00, when both the river discharge and offshore wave heights had decayed and the significant bathymetry change around the river mouth was already caused. In case (iii), therefore, we applied the present numerical model to the same bathymetry measured in August 2007 and instead examined the influence of the equivalent bottom roughness on the discharging river flow. As summarized in Table 2, sub-cases (a), (b) and (c) in case (iii) applied spatially uniform bottom roughness, k_N=0.5mm, 5mm, 50mm, respectively , while case (d) applied spatially varying sheet flow roughness based on Herrmann and Madsen's (2005) model, in which uniform sediment grains of D_{50}=0.5mm were applied. Note that the river discharge rates in cases (i) and (iii) are nearly equivalent to each other.

As seen in Table 2 and Figure 8, increase of bottom roughness from 0.5mm to 50mm decreased predicted surface water elevations about 73cm, which is still smaller than the ones due to different bathymetry conditions. The model showed reasonable predictive skills of the surface water elevations and current velocities when the model applied equivalent bottom roughness of either k_N=5mm or sheet flow roughness. Relatively small underestimation of both surface water elevation and surface water velocity in case (iii) may be due to underestimation of the river discharge because we applied the river discharge estimated at 17:00 at Kashima, about 25km-upstream from the river mouth, and there should be a certain time-lag between Kashima and the river mouth.

As seen in the numerical analysis, the river mouth bathymetry has significant impacts on surrounding wave and current fields. On the other hand, the present image-based observations found that intensive storm waves and flooding currents could deform the river mouth bathymetry within an hour or less, i.e., a relatively short period of time which is comparable to the time scale of the changes in offshore waves and river discharge conditions. It is therefore inevitable to account for interactive features among waves, currents and bathymetry for accurate predictions of their dynamic behaviors. Monitoring time-to-time bathymetry change during the storm is therefore essential to capture the dynamics around the river mouth
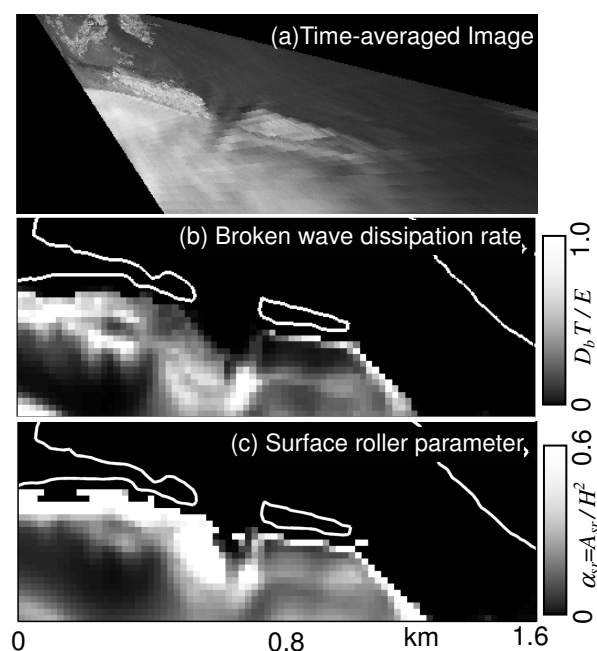
Figure 9 Spatial distributions of (a) rectified time exposure image of pixel intensity (b) predicted surface roller parameter, and (c) predicted broken wave dissipation rate (at 17:00 on July 15th; case (iii)).

while it is virtually difficult to apply conventional direct measurement techniques to obtain such data. To compensate this problem, remote-sensing techniques to monitor the nearshore dynamics have been studied. Lippmann and Holman (1989), for example, developed well-known ARGUS system and monitored nearshore surf zone and underneath bathymetry based on the time exposure video images in which surf zone appears as whitish high intensity image.

This section follows the same concept as Lippmann and Holman (1989) and aims to seek quantitative relationship between the obtained images and certain index parameters computed by the numerical wave model. This quantitative relationship may enable us to inversely estimate bathymetry by matching the image with the parameters computed by the numerical wave model with arbitrary bathymetry conditions. In this study, we introduce two parameters to indicate the surf zone: (i) broken wave dissipation rate, D_b, obtained by integrating $D_{NB}\sigma$ over entire specter and (ii) surface roller parameter, α_{sr}, obtained by normalizing surface roller area, A_{sr}, by local wave height, i.e., $\alpha_{sr}=A_{sr}/H^2$.

Figure 9 compares rectified time-averaged image around the river mouth with predicted broken wave dissipation rate and surface roller parameters. Both image and predicted results are for case (iii) after the sand bar was fully collapsed at 17:00. In the figure, broken wave dissipation rate, D_b, was also normalized by the local wave energy, E, and their significant wave period, T. As seen in the figure, surface roller parameter reasonably represent the spatial distributions of observed whitish surf zone especially in that cross-shore range of the surf zone is wider in the west side of the opened sand bar, whitish surf zone forms "V-shape" surrounding the discharging flow in front of the opened sand bar, and, darker non-breaking area lies just behind (seaside) of the surf zone along the shoreline in the east side of the opened sand bar. In front of the opened sand bar where we observed V-shaped surf zone, directions of the river flow, which is seen in darker area, are slightly different between the image and the predicted surface roller parameter. This feature somehow indicates that the bathymetry conditions used for the numerical computations might have been deformed by the waves after the storm.

6. Conclusions

Interactive features of waves, currents and the river mouth bathymetry change were studied based on successive digital still images taken by six cameras installed around the Tenryu River mouth. The installed camera successfully captured the collapse of the sand bar when the Typhoon T0704 hit the Pacific coast of

Japan in the middle of July 2007. Obtained images were first rectified and combined based on the estimated real world coordinate system to yield overview image of the sand bar at the Tenryu River mouth. Time exposure images were developed by digitally averaging successive images over 10 minutes and the time-to-time changes of the plane shapes of the sand bar was compared with the recorded time-varying river discharge and the surface water levels along the Tenryu River. From the successive still images, drifting debris were traced to estimate the surface water flow velocity during the storm.

It was found from the observed images that the river mouth sand bar was collapsed in two steps. First, the original river mouth opening was widened as the river discharge increased and then the middle-west part of the sand bar was cut as the difference of the surface water elevations between seaside and landside of the sand bar reached its peak. The timing of the abrupt decay of the surface water velocity at the river mouth corresponded to the ones when these two major collapse of the sand bar.

Impact of the river mouth bathymetry on tidal response at the river mouth was also investigated by comparing the difference of the height and timings of the tidal peak at Omaezaki, open sea, and at Ryuyo, behind the sand bar. Both time-lags and elevation difference of the tidal peaks between these two observation site clearly decreased after the storm, i.e., after the cross-section area of the river mouth opening was enlarged.

Numerical analysis was finally applied to further investigate the observed interactive features among waves, currents, and changing bathymetry of the river mouth. The model accounted for wave-current interactions such as Doppler effects of current on breaking and non-breaking waves, wave radiation forces acting on the current and turbulence induced from bottom boundary layer under wave-current coexisting fields. The wave and the current modules were iteratively applied to account for the influence of each other. Sensitivity analysis based on the developed model found the most significant impact of the river mouth bathymetry on the forcing balance at the river mouth compared to the other factors such as bottom frictions and wave radiation forces. Accounting for the appropriate bathymetry conditions, in the other word, the model showed reasonable predictive skills of the current velocity and surface water gradient at the river mouth.

Finally, the time exposure image was compared with the spatial distributions of the predicted broken wave dissipation rate and surface roller parameters and it was found that the proposed surface roller parameter well represents the spatial distributions of the surf zone which appears in whitish color in the obtained time-exposure image.

Acknowledgements

References

Herrmann, M. and O.S. Madsen, 2007. Effect of stratification due to suspended sand on velocity and concentration distribution in unidirectional flows, *J. Geophys. Res.*, vol.112, C02006, 13p.

Holland, K.T., Holman, R.A., Lippmann, T.C. and Stanley, J., 1997. Practical use of video imagery in nearshore oceanographic field studies, *IEEE J. of Ocean. Eng.*, 22(1), pp.81-92.

Larson, M and N. C. Kraus, 1991. Numerical model of longshore current for bar and trough beaches, *J. Waterway, Port, Coastal and Ocean Eng.*, vol.117, No.4, pp.326-347.

Lippmann, T.C., and R.A., Holman, 1989. Quantification of sand bar morphology: A video technique based on wave dissipation. *J. of Geophys. Res.*, 94(C1), 995-1011.

Madsen, O. S., 1994. Spectral wave-current bottom boundary layer flows, *Proc. 24th Int. Conf. on Coast. Eng.*, pp.384-398.

Mase, H., Yuhi, M., Amamori H., and T. Takayama, 2004. Phase averaging wave prediction model with breaking and diffraction effects in wave-current coexisting field. *Annual J. of Coastal Eng.*, JSCE, 51:6-10 (in Japanese).

Tajima, Y., and O. S. Madsen, 2006. Modeling near-shore waves, surface rollers, and undertow velocity profiles, *J. of Waterway, Port, Coastal and Ocean Eng.*, Vol. 132, No. 6, pp. 429-438, 2006.